RESEARCH ARTICLE

National Science Review
5: 642–652, 2018
doi: 10.1093/nsr/nwy048
Advance access publication 17 April 2018

CHEMISTRY

Special Topic: Single-Atom Catalysts

Single-atom heterogeneous catalysts based on distinct carbon nitride scaffolds

Zupeng Chen[1], Evgeniya Vorobyeva[1], Sharon Mitchell[1,*], Edvin Fako[2], Núria López[2], Sean M. Collins[3], Rowan K. Leary[3], Paul A. Midgley[3], Roland Hauert[4] and Javier Pérez-Ramírez[1,*]

[1]Institute for Chemical and Bioengineering, Department of Chemistry and Applied Biosciences, ETH Zurich, 8093 Zurich, Switzerland; [2]Institute of Chemical Research of Catalonia (ICIQ), The Barcelona Institute of Science and Technology, 43007 Tarragona, Spain; [3]Department of Materials Science and Metallurgy, University of Cambridge, Cambridge, CB3 0FS, UK and [4]Empa, Swiss Federal Laboratories for Materials Science and Technology, 8600 Dübendorf, Switzerland

*Corresponding authors. E-mails: sharon.mitchell@chem.ethz.ch; jpr@chem.ethz.ch

Received 5 February 2018; **Revised** 10 April 2018; **Accepted** 13 April 2018

ABSTRACT

Carbon nitrides integrating macroheterocycles offer unique potential as hosts for stabilizing metal atoms due to their rich electronic structure. To date, only graphitic heptazine-based polymers have been studied. Here, we demonstrate that palladium atoms can be effectively isolated on other carbon nitride scaffolds including linear melem oligomers and poly(triazine/heptazine imides). Increased metal uptake was linked to the larger cavity size and the presence of chloride ions in the polyimide structures. Changing the host structure leads to significant variation in the average oxidation state of the metal, which can be tuned by exchange of the ionic species as evidenced by X-ray photoelectron spectroscopy and supported by density functional theory. Evaluation in the semi-hydrogenation of 2-methyl-3-butyn-2-ol reveals an inverse correlation between the activity and the degree of oxidation of palladium, with oligomers exhibiting the highest activity. These findings provide new mechanistic insights into the influence of the carbon nitride structure on metal stabilization.

Keywords: single-atom heterogeneous catalysts, carbon nitride scaffolds, alkyne semi-hydrogenation, density functional theory, metal–host interaction

INTRODUCTION

The exploration of single-atom heterogeneous catalysts (SACs) based on noble metals has been stimulated by the prospect of improving metal utilization and selectivity simultaneously in sustainable catalytic processes [1–6]. Unfortunately, atomically dispersed metals on common hosts (e.g. metals, metal oxides and carbons) are often thermodynamically unstable and aggregate into clusters or nanoparticles, especially at elevated temperature [7]. In this regard, graphitic carbon nitride (herein denoted as GCN) emerges as a unique host for preparing SACs due to the presence of nitrogen-rich macroheterocycles in the lattice, which can anchor metal atoms firmly [8,9]. The density of the adsorption pockets also helps to maintain dispersion by configurational entropy considerations. In comparison to SACs supported on other nitrogen-doped carbons, which typically exhibit significant structural heterogenity, the higher content and uniform type and arrangement of nitrogen species within GCN materials offer abundant and more precisely defined coordination sites.

Graphitic carbon nitride is regarded as the most stable polymorph upon polymerization of common nitrogen-rich precursors (e.g. cyanamide, dicyanamide and melamine) under ambient conditions, and is widely used as a photocatalyst [10–14]. In agreement with density functional theory (DFT) predictions of the higher thermodynamic stability, most experimental studies report the formation of heptazine- rather than triazine-based molecular structures [8,9,15–19]. Since the preparation of GCN is a stepwise polymerization process, various intermediate phases including melam, melem and linear melem oligomers (LMO) can be obtained by

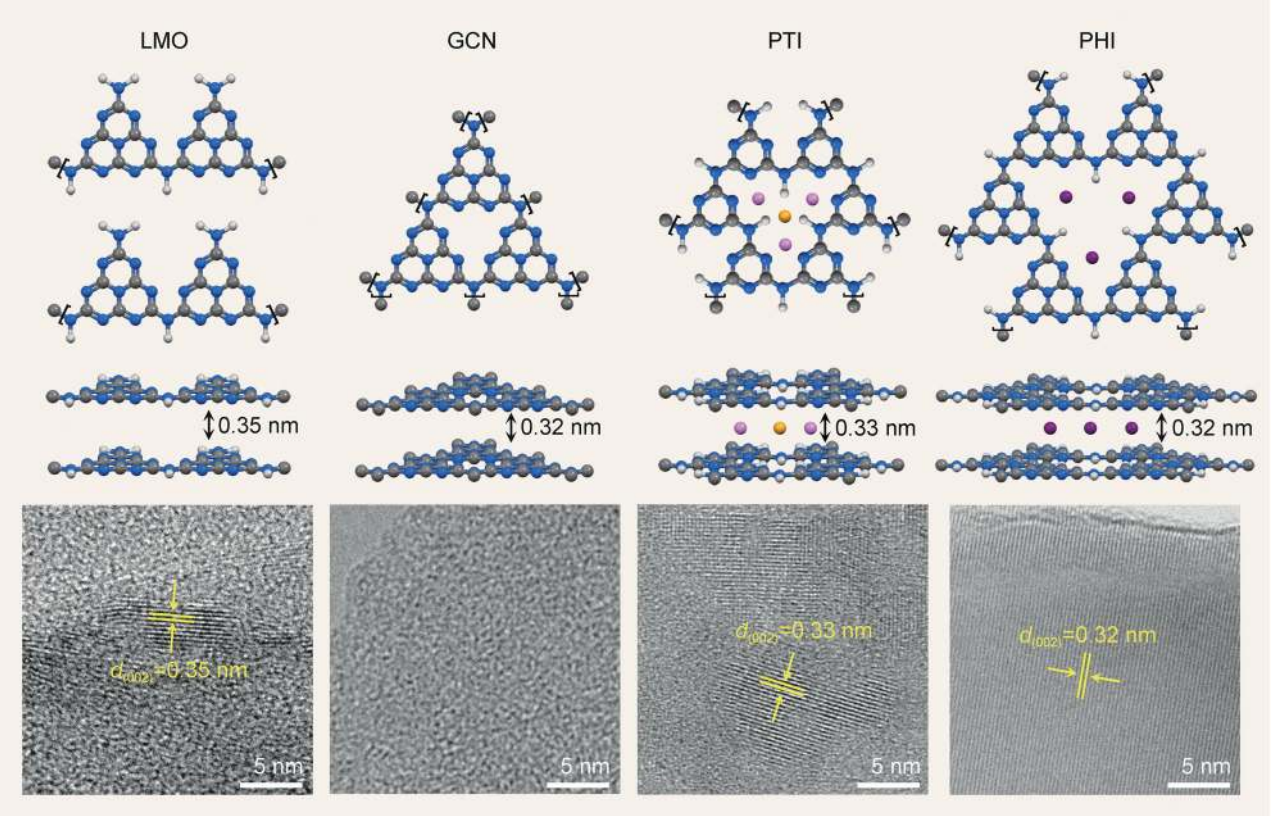

Figure 1. Idealized structure motifs and high-resolution TEM images of LMO, GCN, PTI and PHI. Sites that further polymerize in the extended structure are indicated with parentheses. Color codes: gray, C; blue, N; white, H; pink, Li; purple, K; orange, Cl. The relaxed structures are shown in Supplementary Fig. 16.

varying the synthesis conditions (temperature, pressure or atmosphere) [20,21]. On the other hand, highly crystalline carbon nitrides comprising ordered poly(triazine imide) (PTI) or poly(heptazine imide) (PHI) can be assessed either by increasing the temperature or pressure [22,23] or by ionothermal synthesis employing eutectic salt mixtures of Li*X*/K*X* (X = Cl or Br) [23–26] or simply single alkaline metal chlorides [27,28] as the solvent.

Various metals (Pd, Ag, Pt or Ir) have been stabilized as single atoms on GCN by using both direct (e.g. copolymerization, *in-situ* doping) and post-synthetic (e.g. wet deposition optionally assisted by microwave irradiation and/or combined with chemical reduction) approaches [29–36]. The method of metal introduction is known to impact the distribution of metal centers within the host, the post-synthetic deposition resulting in higher surface metal densities and consequently increased turnover frequencies in the three-phase semi-hydrogenation of alkynes. Furthermore, both the accessibility and electronic properties of adsorbed metal species could also be altered by varying the morphology and porosity of GCN [33]. By doping carbon into the lattice of GCN, we recently reported the controlled variation of the C/N ratio, pointing out the potentially critical role of the strength of the metal–host interaction [35]. However, to date, the preparation of SACs based on other carbon nitrides including LMO and crystalline PTI and PHI phases has not been attempted.

To guide the design of improved SACs and gain insight into the effect of the host structure on metal stabilization, a series of carbon nitride materials (LMO, GCN, PTI and PHI) have been prepared (the idealized structure motifs are illustrated in Fig. 1). The comparative properties of the distinct scaffolds are studied in depth before and after the introduction of palladium via microwave-assisted deposition. The single-atom dispersion is confirmed in all cases by aberration-corrected scanning transmission electron microscopy, while analysis by X-ray photoelectron spectroscopy reveals significant variation in the formal oxidation state of the metal. DFT calculations are conducted to shed further light on the interaction of the metal with the different scaffolds, which is fundamental to understand the performance that in our case was interrogated through the semi-hydrogenation of 2-methyl-3-butyn-2-ol. The possibility to tune the electronic properties of

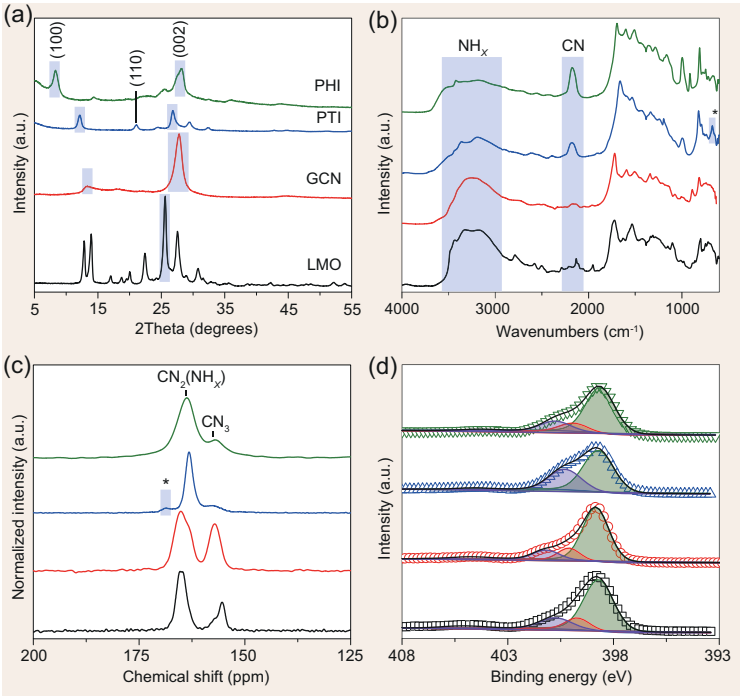

Figure 2. (a) XRD patterns, (b) DRIFTS spectra, (c) ^{13}C CP/MAS NMR spectra and (d) N 1*s* XPS spectra of the investigated carbon nitride scaffolds. The sample color codes in (a) apply to all panels. The transparent blue boxes indicate the reflections and stretching assignments, where the asterisks indicate bands characteristic of the PTI structure. In (d), the black lines show the fitted result of the raw data (open symbols), whereas the green, red and purple peaks corresponding to the deconvoluted C-N = C, NC_3 and -NH_x components.

the metal via the exchange of intercalated ions in the polyimides is also demonstrated.

RESULTS AND DISCUSSION

Host properties

The distinct carbon nitride scaffolds were prepared adapting previously reported protocols [22–25,37]. In particular, LMO and GCN were obtained by direct polymerization of melamine at different temperatures, while PTI and PHI were synthesized by a similar approach exploiting eutectic salt mixtures of LiCl/KCl as the solvent. Analysis by X-ray diffraction (XRD) confirms the characteristic crystalline structures of the resulting materials (Fig. 2a). In particular, GCN exhibits an intense reflection at 27.3° 2θ (002) associated with the graphite-like interlayer stacking and a weak in-plane reflection stemming from heptazine repeating units at 13.1° 2θ (100). PTI features a number of well-resolved reflections, which are consistent with the expected hexagonal structure and $P6_3cm$ space group [23]. The strongest reflection at 26.8° 2θ indexed as the (002) plane corresponds to an interlayer distance of 0.33 nm, whereas the (002) reflection of PHI was found to be at 26.2° 2θ (0.32 nm). Note that the reflection at 12.2° 2θ of PTI corresponding to the (100) in-plane periodicity shifts to a lower angle (8.3° 2θ) in PHI. In the case of LMO, the XRD pattern agrees well with previously reported observations, where the (002) reflection at 25.5° 2θ features an interlayer distance of 0.35 nm [37]. The high crystalline order of the carbon nitride hosts was further evidenced by high-resolution transmission electron microscopy (TEM) imaging (Fig. 1). Although not observed in GCN due to the in-plane structural disorder and beam sensitivity, LMO, PTI and PHI exhibited lattice fringes with spacings of 0.35, 0.33 and 0.32 nm, respectively, corresponding to the (002) planes in these stacked aromatic structures. Additional lattice fringes with distances of 0.44 and 0.74 nm were also observed in the case of PTI (Supplementary Fig. 1), which can be assigned to the (110) and (100) planes, respectively.

The distinct structures were further corroborated by diffuse reflectance infrared Fourier transform spectroscopy (DRIFTS), ^{13}C solid-state cross-polarization/magic angle spinning nuclear magnetic resonance (CP/MAS NMR) spectroscopy and X-ray photoelectron spectroscopy (XPS). The DRIFTS spectra (Fig. 2b) evidence the existence of the aromatic heterocycles in all hosts, showing the stretching at 1100–1650 cm^{-1}, while the broad bands at 3000–3300 cm^{-1} are assigned to the bending of -NH_x terminations [38]. Though bearing the same building units of heptazine, LMO shows more intense -NH_x breathing modes than GCN, indicative of more peripheral -NH_x terminations in LMO. The cumulated double bonds (-N=C=N-) at 2184 cm^{-1} are obvious in PTI and PHI, evidencing the presence of -NH- bridges as in ketene imines [39]. In addition to the deformation vibrations of the triazine or heptazine rings at 814 cm^{-1}, a unique band at 670 cm^{-1} in PTI suggests that triazine rings are the building units [23,40], instead of the heptazine in the other cases. LMO and GCN show similar ^{13}C NMR spectra (Fig. 2c) with two main peaks at 164 and 155–157 ppm, attributed to $CN_2(NH_x)$ and CN_3 moieties, respectively. These signals are also present in PTI and PHI, but the ratio between the intensity at 164 and 157 ppm is much higher, demonstrating more carbon species close to periphery -NH_x. On the other hand, an additional peak at 168 ppm indicates the presence of triazine rings in PTI, which can be ascribed to the carbons with few protons in its proximity [41]. Furthermore, the main contribution at 288.3 eV in the C 1*s* XPS spectra (Supplementary Fig. 2) originates from the carbon species in the triazine or heptazine rings. Comparatively, deconvolution of N 1*s* spectra (Fig. 2d)

Table 1. Characterization data of the carbon nitride scaffolds and associated SACs.

Host[a]	Formula[b]	S_{BET}[c] ($m^2\ g^{-1}$)	Pd[b] (wt.%)	Loading efficiency[d] (%)	Pd surface density[e] ($\mu mol_{Pd}\ m^{-2}$)
LMO	$C_3N_{4.86}H_{2.69}O_{0.11}$	3 (29)	0.66	33	8.6
GCN	$C_3N_{4.64}H_{1.59}O_{0.10}$	8 (11)	0.58	29	63.8
PTI	$C_3N_{4.52}H_{2.89}O_{0.82}Li_{0.16}K_{0.05}Cl_{0.12}$	68 (76)	0.56	100	1.7
PHI	$C_3N_{4.27}H_{3.11}O_{1.43}Li_{0.04}K_{0.27}Cl_{0.01}$	31 (30)	0.47	95	4.7
PTI-Mg	$C_3N_{4.55}H_{2.96}O_{0.84}Li_{0.15}K_{0.01}Cl_{0.08}Mg_{0.02}$	80 (110)	0.50	100	1.6
PHI-Mg	$C_3N_{4.36}H_{3.38}O_{1.49}Li_{0.00}K_{0.09}Cl_{0.01}Mg_{0.10}$	31 (40)	0.48	96	4.2

[a]LMO, linear melem oligomer; GCN, graphitic carbon nitride; PTI, poly(triazine imide); PHI, poly(heptazine imides); PTI-Mg and PHI-Mg, magnesium ion-exchanged PTI and PHI.
[b]Determined by elemental analysis (non-metals) or ICP-OES (metals).
[c]BET method (in parentheses, the surface area of the SACs).
[d]Determined by 100 × (actual metal content/targeted metal content).
[e]Determined from the surface Pd concentration (from XPS) and area (from gas sorption) of the SACs.

of LMO, GCN and PHI evidence three main peaks at 398.8, 399.9 and 401.0 eV, which can be ascribed to the ring nitrogen (C-N = C), tertiary nitrogen (NC_3) and terminal -NH_x groups. The ratio of C-N=C/NC_3 was calculated to be around 6, confirming the presence of heptazine as the building unit [25]. Taking account of the relative nitrogen content from elemental analysis (Table 1), the surface NH_x concentration for LMO was calculated to be 6.8 mmol g^{-1}, which is 1.3-fold more than that of GCN (5.3 mmol g^{-1}). On the other hand, the absence of the tertiary nitrogen (NC_3) and the C-N=C/NC_3 ratio of around 2, accompanied by some shift in the terminal -NH_x, suggest again that the obtained PTI is built of triazine instead of heptazine units.

The chemical composition of the hosts was determined by elemental analysis and inductively coupled plasma-optical emission spectrometry (ICP-OES) (Table 1). The C/N molar ratio of LMO is 0.62, which is lower than its GCN counterpart (0.65), likely due to the abundant -NH_x terminations in LMO. Meanwhile, the C/N ratios of PTI and PHI are 0.66 and 0.70, respectively, which are very close to the theoretical values (0.67 for PTI and 0.71 for PHI). The Li, K, Cl molar contents (in mol.%) in PTI and PHI (PTI/PHI) were calculated to be 2.3/0.3, 0.5/2.2 and 1.0/0.1, respectively. Therefore, it can be concluded that PTI is intercalated by Li^+ and Cl^- simultaneously, while PHI is preferentially intercalated with K^+. The presence of exchangeable ions in PTI and PHI offers a further possibility to tune the electronic properties of the hosts. Magnesium was chosen as the exchanged species, since Mg^{2+} is known to interact well with the N species in porphyrins and it has a comparable or smaller ionic radius (r_{ion} = 86 pm) than that of the Li^+ (90 pm) and K^+ (152 pm) ions initially present in the structures. As shown in Table 1, only 0.41 wt.% Mg was exchanged into the framework of PTI, while the Mg content can be introduced into PHI up to 1.94 wt.%, indicating that K^+ in PHI can be efficiently exchanged with Mg^{2+}. The structure of PTI and PHI remains unchanged upon Mg^{2+} exchange, as suggested by the similarity of the XRD patterns (Supplementary Fig. 3).

The distinct morphology of the applied hosts was visualized by TEM and scanning electron microscopy (SEM) (Supplementary Fig. 4). In contrast to the irregularly shaped LMO and GCN, PTI displays fiber-like morphology constituted by cubic and hexagonal nanocrystals, while PHI presents a mixture of rod-like structures and plates. As evidenced by argon sorption (Supplementary Fig. 2), PTI and PHI exhibit higher surface areas (68 and 31 $m^2\ g^{-1}$, respectively) than non-porous LMO and GCN (3 and 8 $m^2\ g^{-1}$, respectively), which is linked to the nanostructured characteristics of the polyimide structures.

Metal stabilization

To study the capacity of the distinct carbon nitride scaffolds as hosts for single atoms, palladium was introduced via a microwave-assisted deposition targeting a loading of 2 wt.%. Increased metal deposition was observed for the polyimide structures, taking up 66% (PTI) and 68% (PHI) of the available metal leading to palladium contents of 1.32 and 1.35 wt.%, respectively. Comparatively, lower uptakes 33% (LMO) and 29% (GCN) were observed for the other carbon nitrides (incorporating 0.66 and 0.58 wt.%, respectively). This is tentatively attributed to the specific binding of palladium by the former carriers (*vide infra*) although the higher surface area of these materials could also enhance the capacity as a metal host. For an improved catalytic evaluation, two additional SACs based on PTI

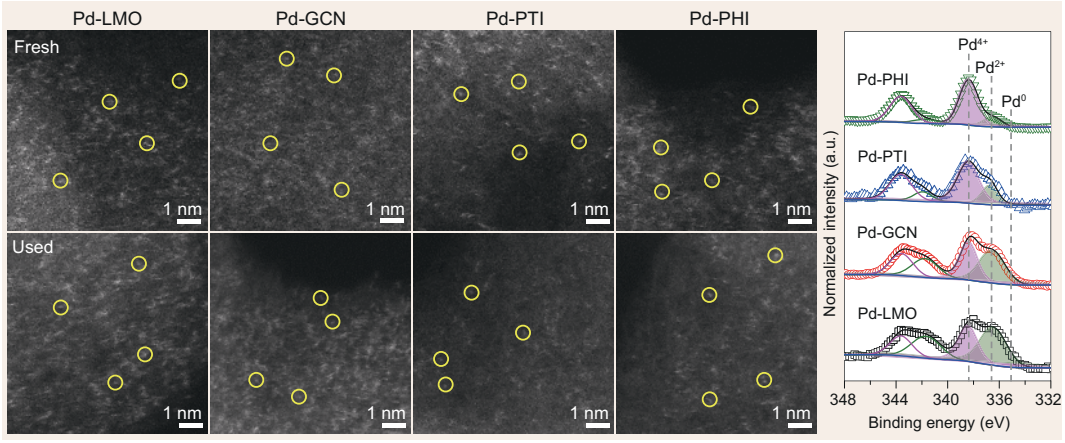

Figure 3. AC-HAADF-STEM images of the fresh and used Pd-SACs based on different carbon nitride scaffolds and Pd 3*d* core-level XPS spectra of the fresh catalysts. Some isolated Pd atoms are identified by yellow circles. Additional low-magnification HAADF-STEM images of the fresh samples are shown in Supplementary Fig. 17. In the XPS spectra, the black lines show the fitted result of the raw data (open symbols), whereas the magenta and green peaks correspond to the deconvoluted components. The dashed lines indicate the positions formally assigned to Pd^{4+}, Pd^{2+} and Pd^{0} species.

and PHI were prepared with metal contents close to 0.5 wt.% (Table 1).

The examination by aberration-corrected high-angle annular dark-field scanning transmission electron microscopy (AC-HAADF-STEM) verified the single-atom dispersion of palladium, where the higher-atomic-number metal atoms are visible as the sub-nanometer bright spots on a smoothly varying gray background signal from the lower-atomic-number hosts (Fig. 3 and Supplementary Fig. 5). To assess the macroscopic metal distribution, thin cross-sections of the embedded materials were mapped by energy-dispersive X-ray (EDX) spectroscopy, indicating a relatively uniform presence of palladium throughout LMO, PTI and PHI (Supplementary Fig. 6). In contrast, a surface enrichment in the concentration of palladium was observed for GCN, suggesting that the metal is unable to penetrate deeply into the material.

The influence of the host structure on the electronic properties of palladium was studied by XPS. The presence of two different oxidation states was clearly distinguishable from the Pd 3*d* core-level spectra (Fig. 3), at around 338.3 and 336.5 eV, respectively. Based on formal assignments, these peaks can be attributed to Pd^{4+} (338.3 eV) and Pd^{2+} (336.5 eV). Notably, no signal corresponding to the metallic Pd fingerprint (appearing at 334.9 eV) was detected in any of the catalysts. These observations are consistent with the expected strong interaction between the isolated atoms and hosts and the absence of nanoparticles evidenced by microscopy. Notice that the direct assignment of formal charges is debatable, and the values above are only used for reference purposes indicating the existence of palladium species with differing degrees of oxidation or coordination to atoms with different electronegativity. Significant variation of the ratio of Pd^{2+}/Pd^{4+} was observed, ranging from 0.19 (Pd-PHI) and 0.31 (Pd-PTI) to 1.04 (Pd-GCN) and 1.32 (Pd-LMO), indicating that the strength of the metal–host interaction can be manipulated depending on the framework structure of carbon nitrides. The relatively high contribution of Pd^{4+} in PTI and PHI is rationalized by the possible interaction of palladium with intercalated ionic species in these materials (*vide infra*). To assess the chemical state of sub-surface palladium atoms in the SACs, a depth-profiling analysis by XPS coupled with Ar^{+} beam etching was conducted to remove the surface layer (Supplementary Fig. 7). In all cases, the Pd 3*d* core-level spectra are slightly shifted to higher binding energies, showing an evolution towards Pd^{4+}. The charge assignment is done by comparison with standards and thus they might differ from the charges obtained in the DFT calculations.

To gain insight into the relative thermal stability, the distinct Pd-SACs were treated both in air at 673 K and in a flowing 5%H_2/He mixture at 433 K, the latter conditions representative of those typically employed in gas-phase hydrogenation reactions [32,42]. The Pd atoms over LMO, PTI and PHI exhibit high resistance to sintering with no sign of nanoparticle formation (Supplementary Fig. 8), while abundant Pd clusters become visible at the surface of GCN. The lower stability of single atoms over GCN can be due to several reasons. Comparatively, Pd atoms bind weakly to GCN, as evidenced by the lowest average oxidation state of the metal observed by XPS and supported by DFT calculations (*vide infra*). In addition, the surface density of metal

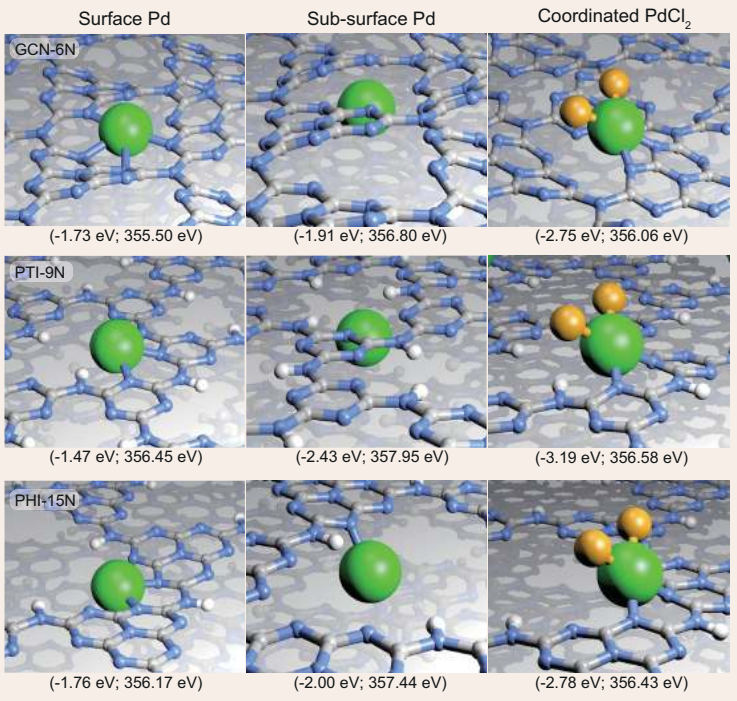

Figure 4. Optimized Pd coordination sites within different carbon nitride scaffolds with 6 N, 9 N and 15 N pockets. Values in parentheses beneath each image indicate the corresponding formation energies (left), calculated versus an isolated Pd atom or $PdCl_2$ coordination and the relaxed scaffold (the chlorinated system contains Mg^{2+} counter cations between planes) and the calculated Pd 3*d* XPS assignments (right), respectively. The top view representations are shown in Supplementary Fig. 18. Coordinated $PdCl_2$ within GCN was calculated for reference purposes despite the absence of Cl^- in GCN. Color codes: gray, C; blue, N; white, H; green, Pd; orange, Cl.

atoms in the case of GCN is significantly higher compared to the other hosts (Table 1), which could also contribute to their lower stability under thermal treatment. No reflections associated with Pd phases are observed in the XRD patterns (Supplementary Fig. 9) after calcination, in agreement with the preserved high dispersion in all cases. Note that, in the case of LMO, the appearance of a reflection at 6.3° 2θ and the merging of the reflections at around 12.6 and 27.4° 2θ after calcination indicate the likely formation of a new layered complex, which could have a similar structure to previously reported complexes between melamine and cyanuric acid [43]. On the other hand, the disappearance of the in-plane reflection peak at 8.3° suggests a lower stability in the case of PHI.

DFT calculations

DFT has been employed to gain insight into the stabilization of palladium in the distinct carbon nitride scaffolds and their speciation in terms of Bader charge and XPS shift (Fig. 4, Supplementary Table 2 and Supplementary Discussion). The optimized lattices present cavities with different numbers of nitrogen atoms (denoted as 6 N, 9 N and 15 N pockets for GCN, PTI and PHI, respectively). The small 6 N cavity in GCN can efficiently stabilize Pd in the center of the pocket (Pd-6 N) or alternatively by coordinating with four N atoms (Pd-4 N) between two neighboring planes. In the case of the larger cavities (9 N and 15 N), Pd is found to adsorb close to two N centers. A consistent range of Pd 3*d* shift was noticed during the simulation of the XPS profiles. In general, the Pd atoms preferentially reside at the subsurface layer of carbon nitrides, particularly for PTI. For all scaffolds, the surface Pd appears to be the least oxidized (Pd^{2+}) and they are suggested to be more active than their more oxidized counterparts (Pd^{4+}) that are buried more deeply in the material (especially in the case of PTI and PHI) and therefore less accessible, which is consistent with the XPS depth-profiling analysis. In the presence of chlorine, palladium can coordinate in the form of PdN_2Cl_2 that is also more oxidized than their surface counterparts. The $PdCl_2$ are less likely in the smallest cavities, as they imply a larger perturbation in the scaffold. The presence of Cl^- negatively affects the activity, since it lowers the *d*-band position of the Pd levels (Supplementary Table 2) and it would be necessary to cleave Pd-Cl bonds (energetically more favorable than cleavage of Pd-N bonds) to adsorb reactants. Furthermore, the incorporation of Mg^{2+} in the subsurface vacancy of PTI and PHI steadily propels the Pd species to the surface, which would be expected to positively influence the activity. *Ab-initio* molecular dynamics (MD) simulations were conducted on Pd-GCN, highlighting the high stability of this system. Upon increasing the temperature, the Pd atoms are observed to fluctuate between the surface (less oxidized) and subsurface (more oxidized) configurations (Supplementary Fig. 10). The stability of the Pd-SACs was further assessed in the presence of O_2 or H_2, sampling the potential energy surface with relevant intermediates (Supplementary Fig. 11). In all cases, the adsorption of oxygen is found to have a stabilizing effect. Two distinct scenarios are observed for the activation of hydrogen, which is found to occur homolytically, resulting in improved stability of the single atoms on PTI and PHI, but occurs heterolytically, slightly weakening the coordination of Pd (by 0.24 eV), on GCN with smaller cavity. The adsorption energy of 2-methyl-3-butyn-2-ol was probed, confirming the preferred interaction with surface sites (Supplementary Table 3).

Alkyne semi-hydrogenation performance

The catalytic performance was evaluated in the semi-hydrogenation of 2-methyl-3-butyn-2-ol,

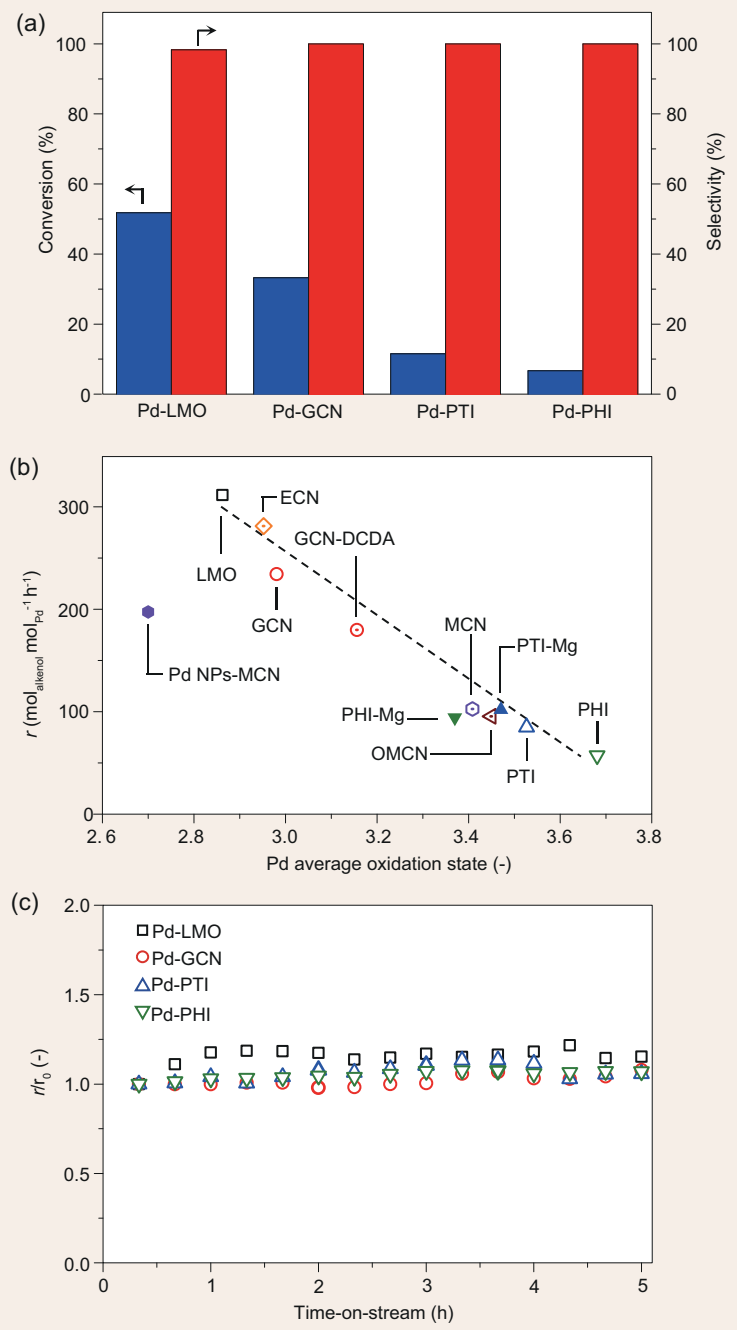

Figure 5. (a) Conversion and selectivity to 2-methyl-3-buten-2-ol in the hydrogenation of 2-methyl-3-butyn-2-ol of Pd-SACs based on carbon nitride scaffolds of different lattice structure. (b) Correlation of the rate of 2-methyl-3-buten-2-ol formation with the palladium average oxidation state. This trend was generalized by considering additional Pd-SACs based on carbon nitrides with different morphology and ion-exchanged form, and the nanoparticle-based catalyst on a mesoporous carbon nitride host. The metal loading was ~0.5 wt.% in all cases. Characterization data of the additional samples is shown in Supplementary Table 1. (c) The relative rate (r/r_0) as a function of time-on-stream over Pd-SACs based on different carbon nitride scaffolds.

which is an important reaction in fine-chemical manufacturing [44]. Despite comparable metal contents of the examined SACs, Pd-LMO exhibits a significantly higher conversion (52%) than other catalysts (Pd-GCN, 33%; Pd-PTI, 11%; Pd-PHI, 7%) (Fig. 5a). Under the conditions investigated, the selectivity towards 2-methyl-3-buten-2-ol approaches 100% over all samples, evidencing the high chemoselectivity of isolated single atoms. As presented in Fig. 5b, the rate of alkenol (2-methyl-3-buten-2-ol) formation is well correlated with the average oxidation state of palladium (Pd_{avg}). For instance, the rate over Pd-LMO with the lowest Pd_{avg} of 2.86 reaches 311 $mol_{alkenol}$ mol_{Pd}^{-1} h^{-1}, which is more than five times higher than that observed over Pd-PHI (57 $mol_{alkenol}$ mol_{Pd}^{-1} h^{-1}) with a Pd_{avg} of 3.68. These findings suggest the critical role of tuning the electronic properties of the host structure in tailoring the strength of metal–host interaction. The stability of the SACs was further evaluated in continuous mode in order to exclude the effects of deactivation due to Pd leaching or aggregation. Importantly, all Pd-SACs display a constant rate towards 2-methyl-3-buten-2-ol formation for 5 h on stream with no variation in conversion or selectivity (Fig. 5c). As additional references, four SACs based on GCN were specifically prepared from different precursor (dicyandiamide (DCDA)) and different morphology (exfoliated, mesoporous and ordered mesoporous carbon nitride (denoted as ECN, MCN and OMCN)) (Supplementary Table 1). Impressively, the rates towards 2-methyl-3-buten-2-ol also fall in the same correlation, despite presenting distinct morphology and single-atom distribution. Although it cannot be assessed by standard techniques, the abundant -NH_x terminations over the oligomer were suggested to improve the accessibility of the active Pd centers. Analysis of the used catalysts confirms the virtually identical atomic dispersion (Fig. 3), electronic properties (Supplementary Fig. 12 and Supplementary Table 4) and crystalline structure (Supplementary Fig. 13) compared to the fresh materials, verifying the stability of the SACs. For reference, the traditional catalyst for the liquid-phase selective hydrogenation of alkynes based on supported lead-modified palladium nanoparticles (Lindlar catalyst, 5 wt.% Pd-3 wt.% $Pb/CaCO_3$) was evaluated as a benchmark. While this catalyst yields a slightly higher rate towards 2-methyl-3-buten-2-ol (517 $mol_{alkenol}$ mol_{Pd}^{-1} h^{-1}), it exhibits significantly reduced selectivity (78% to 2-methyl-3-buten-2-ol) due to over-hydrogenation (22% selectivity to 2-methyl-3-butan-2-ol). This further highlights the superior performance of the

SACs (>95% selectivity to 2-methyl-3-buten-2-ol). To address the impact of magnesium incorporation on the catalytic performance, ∼0.5 wt.% Pd was introduced into PTI-Mg and PHI-Mg (Table 1, Supplementary Fig. 3 and Supplementary Fig. 14). The alkenol formation rates over Pd-PTI-Mg and Pd-PHI-Mg are 102 and 94 $mol_{alkenol}$ mol_{Pd}^{-1} h^{-1}, respectively, which is 1.2 and 1.6 times better compared to those without Mg^{2+} incorporation, while the selectivity towards 2-methyl-3-buten-2-ol is 100% all samples. Again, the reaction rates also correlate with the palladium average oxidation state (Fig. 5b), which further demonstrates the impact of tuning metal–host interaction by tailoring the electronic properties of carbon nitride scaffolds. For comparative purposes, a nanoparticle-containing catalyst based on a mesoporous carbon nitride host (Pd NPs-MCN, with average Pd oxidation state of 2.7; see STEM image in Supplementary Fig. 15) was prepared. Evaluation of this material evidenced a lower rate towards 2-methyl-3-buten-2-ol than the expected trend (Fig. 5), which is consistent with the different metal speciation in this catalyst.

CONCLUSIONS

This study demonstrated the obtainment of SACs on three previously unreported carbon nitride scaffolds, namely linear melem oligomers poly(triazine imides) and poly(heptazine imides). The larger cavity size and presence of chloride ions in the polyimide structures facilitate the accommodation of palladium and enhance the metal–host interaction and thus higher resistance to sintering. An inverse correlation is observed between the activity for semi-hydrogenation of 2-methyl-3-butyn-2-ol and the degree of oxidation of palladium, where the oligomers exhibit the highest activity. This was further generalized over additional previously reported materials, highlighting the critical importance of controlling the oxidation state of isolated metal atoms. The intercalated alkaline metals within the network of PTI and PHI were demonstrated to be able to exchange with other ions such as magnesium, presenting another opportunity to tune the catalytic performance in hydrogenation. The least oxidized surface Pd^{2+} species are suggested to be more active than the Pd^{4+} species that reside deeper in the material; however, this high positive charge can also appear if some ligand remains as PdN_2Cl_2 coordination appears. The findings provide an opportunity to systemically design effective SACs to boost the atom efficiency at an atomic level by constructing the host lattice structure.

METHODS

Carbon nitride synthesis

LMO and polymeric GCN were prepared by calcining melamine (8 g) at the desired temperature (723 K for LMO and 823 K for GCN with a ramp rate of 2.3 K min^{-1}) in a crucible for 4 h under a nitrogen flow (15 cm^3 min^{-1}). PTI and PHI were prepared by ball milling eutectic salt mixtures of LiCl (4.52 g)/KCl (5.48 g) together with a corresponding precursor (melamine (1 g) for PTI and 3-amino-1,2,4-triazole-5-thiol (2 g) for PHI) for 10 min, in a Retsch PM 100 bioMETA planetary ball mill (500 rpm). Afterwards, the mixtures were transferred into a crucible and calcined at 823 K for 4 h (ramp rate, 2.3 K min^{-1}) under a nitrogen flow (15 cm^3 min^{-1}). The resulting products were washed with hot water for 48 h to remove any excess salts. Finally, the carbon nitride products were collected by filtration, washed thoroughly with distilled water and ethanol, and dried at 338 K overnight.

Metal introduction by microwave-assisted deposition

Different carbon nitride hosts (0.5 g) was first dispersed in H_2O (20 cm^3) under sonication for 1 h. Then, an aqueous solution of $Pd(NH_3)_4(NO_3)_2$ containing 5 wt.% Pd (0.05 cm^3, targeting 0.5 wt.%; 0.2 cm^3, targeting 2 wt.%) was added and stirred overnight for complete adsorption. The resulting solution was placed in a microwave reactor (CEM Discover SP), applying a cyclic program (20 repetitions) of irradiation (15 s) and cooling (3 min) using a power of 100 W. The resulting powder was collected by filtration, washed with distilled water and ethanol, and dried at 333 K overnight.

Ion exchange

In a typical synthesis, PTI or PHI (0.7 g) was dispersed in an aqueous solution of $MgCl_2{\cdot}6H_2O$ (3.4 g, 20 cm^3) and then stirred at room temperature for 24 h, after which the solids were collected by centrifugation. These steps were repeated three times and the products were thoroughly washed with water and ethanol, and subsequently dried at 338 K overnight. The samples are denoted as PTI-Mg and PHI-Mg.

Characterization

XRD was performed in a PANalytical X'Pert PRO-MPD diffractometer operated in Bragg-Brentano geometry using Ni-filtered Cu Kα ($\lambda = 0.1541$ nm)

radiation. Data were recorded in the range of 5–60° 2θ with an angular step size of 0.05° and a counting time of 2 s per step. DRIFTS was performed using a Bruker Optics Vertex 70 spectrometer equipped with a high-temperature DRIFT cell (Harrick) and an MCT detector. The samples were pretreated at 423 K for 1 h under Ar before analysis. Spectra were recorded in the range of 4000–400 cm^{-1} under Ar flow (20 cm^3 min^{-1}) and at room temperature by co-addition of 64 scans with a nominal resolution of 4 cm^{-1}. The ^{13}C solid-state cross-polarization/magic angle spinning nuclear magnetic resonance (CP/MAS NMR) spectra were recorded on a Bruker AVANCE III HD NMR spectrometer at a magnetic field of 16.4 T corresponding to a ^1H Larmor frequency of 700.13 MHz. A 4-mm double resonance probe head at a spinning speed of 10 kHz was used for all experiments. The ^{13}C spectra were acquired using a cross-polarization experiment with a contact time of 2 ms and a recycle delay of 1 s. A total of 64×10^3 scans were added for each sample. Between 39×10^3 and 96×10^3 scans were acquired, depending on the sample. The ^{13}C experiments used high-power ^1H decoupling during acquisition using a SPINAL-64 sequence. X-ray photoelectron spectroscopy (XPS) was performed in a Physical Electronics Instruments Quantum 2000 spectrometer using monochromatic Al Kα radiation generated from an electron beam operated at 15 kV and 32.3 W. The spectra were collected under ultra-high vacuum conditions (residual pressure $= 5 \times 10^{-8}$ Pa) at a pass energy of 46.95 eV. All spectra were referenced to the C 1*s* peak of ternary carbon at 288.3 eV. Prior to peak deconvolution, X-ray satellites and inelastic background (Shirley type) were subtracted for all the spectra. The Pd average oxidation state was calculated based on the relative content determined by the peak area of different palladium species from Pd 3*d* core-level XPS spectra. Elemental analysis was determined by infrared spectroscopy using a LECO CHN-900 combustion furnace. Inductively coupled plasma-optical emission spectrometry (ICP-OES) was conducted using a Horiba Ultra 2 instrument equipped with photomultiplier tube detection. The samples were dissolved in a piranha solution and left under sonication until the absence of visible solids in the solution. SEM images were acquired using a Zeiss ULTRA 55 operated at 5 kV. Argon sorption was measured at 77 K in a Micrometrics 3Flex instrument, after evacuation of the samples at 423 K for 10 h. The specific surface area was determined via the Brunauer-Emmett-Teller (BET) method. Samples for TEM studies were prepared by dusting respective powders onto lacey-carbon-coated copper or nickel grids. High-resolution TEM, conventional STEM, and energy-dispersive X-ray spectroscopy (EDX) measurements were performed on a Talos F200X instrument operated at 200 kV and equipped with an FEI SuperX detector. Thin cross-sections were prepared by embedding the powder in a suitable resin (Polysciences Inc., Hard Grade) followed by cutting the sections (100 nm) with a diamond knife. The sections were mounted on carbon-coated copper grids. AC-HAADF-STEM was performed using an FEI Titan^3 80–300 (Thermo Fisher Scientific) microscope equipped with a high-brightness extreme field emission gun and a CEOS (Corrected Electron Optical Systems GmbH) aberration corrector for the probe-forming lenses, operated at 300 kV. The AC-STEM images were acquired with an illumination semi-angle of 18 mrad and a detector inner semi-angle greater than 35 mrad, chosen to minimize any possible Bragg diffraction contrast and maximize overall image signal and especially atomic number (Z) contrast between Pd atoms/clusters and the underlying support. Images were obtained in suitably thin regions of the specimen for minimal background from the support and for reduced overlap of Pd atoms. Per-pixel dwell times of 5–10 μs and probe currents of 40–60 pA were selected to achieve sufficient signal-to-noise for single Pd atom visibility whilst minimizing beam-induced changes, providing images representative of the Pd atom species and their distribution on the LMO, GCN, PTI and PHI hosts.

Hydrogenation of 2-methyl-3-butyn-2-ol

The hydrogenation was carried out in a microwave reactor (CEM Discover SP) with a pressure-controlled vessel under continuous stirring. In a typical reaction, the feed solution containing 0.4 M substrate in toluene (1.5 cm^3) was microwaved in the presence of the catalyst (15 mg) for 1 h at 323 K. The initial hydrogen pressure was 3 bar in all experiments. The resulting reaction mixture was filtered (pore size, 0.45 μm) and the products were collected. The continuous tests were carried out in a flooded-bed micro-reactor (ThalesNano H-Cube Pro^{TM}), in which the liquid-feed-containing 0.4-M substrate in toluene and gaseous hydrogen (generated *in situ* by Millipore water electrolysis) flowed concurrently upward through a cylindrical cartridge (3.5-mm internal diameter) containing a fixed bed of catalyst (0.1 g) and silicon carbide (0.2 g) particles, both with a size of 0.2–0.4 mm. The reactions were conducted at $T = 323$ K, $P =$ 3 bar, liquid (1 cm^3 min^{-1}) and H_2 (36 cm^3 min^{-1}) flow rates. The products were collected every 20 min after reaching steady state. All collected samples

were analyzed offline using a gas chromatograph (HP-6890) equipped with a HP-5 capillary column and a flame ionization detector. The conversion (X) of the substrate was determined as the amount of reacted substrate divided by the amount of substrate at the reactor inlet. The selectivity (S) to each product was quantified as the amount of the particular product divided by the amount of reacted substrate. The reaction rate (r) was expressed as the number of moles of product formed per mole of Pd and unit of time.

DFT simulations

Slab models representing different carbon nitride scaffolds have been described through the DFT as implemented in the Vienna Ab initio Simulation Package (VASP) code [45], using the Perdew-Burke-Ernzerhof (PBE) functional together with D3 dispersion terms [46,47]. Core electrons were replaced by projector augmented wave (PAW) method [48] and the valence electrons were expanded in plane waves with a kinetic cut-off energy of 450 eV. The bulk structures were derived from our previous carbon nitride system by expanding the building motifs. The *k*-point densities were 5 × 5 × 5 for GCN and PTI system and 3 × 3 × 5 for PHI. Slab models were cut along the van der Waals planes; the slabs contain four layers and are interleaved by at least 12 Å of vacuum. The optimized crystal lattices are presented in the Supplementary Material. The *k*-point sampling in these cases was 3 × 3 × 1 (GCN and PTI) and 1 × 1 × 1 (PHI). The $PdCl_2$ precursor and Pd atoms were anchored at different positions in the cavities and within the two uppermost layers, which are preferential sites for the simplest carbon nitrides as observed in first-principles MD. The Heyd-Scuseria-Ernzerhof (HSE03) [49] functional was used to generate the partial density of states (PDOS) of the relaxed structures, including 25% of exact Hartree-Fock exchange. *Ab-initio* MD simulations were conducted on the Perdew-Burke-Ernzerhof (PBE) level, and comprised heating/equilibration cycles in which the system was heated to 500 K with a cycle step of 100 K for a total duration of 10 ps. The structures can be retrieved from the ioChem-BD database [50] at the following dataset: DOI:10.19061/iochem-bd-1-75.

SUPPLEMENTARY DATA

Supplementary data are available at *NSR* online.

ACKNOWLEDGEMENTS

ScopeM at ETH Zurich for access to its facilities. The service of Microelemental Analysis at ETH Zurich for CHN analysis. BSC-RES for providing generous computational resources. Dr R. Verel for NMR measurements. Dr A.J. Martın for SEM measurements.

FUNDING

This work was supported by ETH Zurich, the Swiss National Science Foundation (200021–169679), the Spanish Ministerio de Economía y Competitividad (CTQ2015–68770-R) and the European Research Council under the European Union's Seventh Framework Program (291522–3DIMAGE). E.F. thanks the Spanish Ministerio de Economía y Competitividad (MINECO) La Caixa-Severo Ochoa for a pre-doctoral grant through Severo Ochoa Excellence Accreditation 2014–2018 (SEV-2013–0319). S.M.C. acknowledges support from the Henslow Research Fellowship at Girton College, Cambridge.

Conflict of interest statement. None declared.

REFERENCES

1. Qiao B, Wang A and Yang X *et al.* Single-atom catalysis of CO oxidation using Pt_1/FeO_x. *Nat Chem* 2011; **3**: 634–41.
2. Kamiya K, Kamai R and Hashimoto K *et al.* Platinum-modified covalent triazine frameworks hybridized with carbon nanoparticles as methanol-tolerant oxygen reduction electrocatalysts. *Nat Commun* 2014; **5**: 5040.
3. Lucci FR, Liu J and Marcinkowski MD *et al.* Selective hydrogenation of 1,3-butadiene on platinum-copper alloys at the single-atom limit. *Nat Commun* 2015; **6**: 8550.
4. Wei H, Liu X and Wang A *et al.* FeO_x-supported platinum single-atom and pseudo-single-atom catalysts for chemoselective hydrogenation of functionalized nitroarenes. *Nat Commun* 2014; **5**: 5634.
5. Kyriakou G, Boucher MB and Jewell AD *et al.* Isolated metal atom geometries as a strategy for selective heterogeneous hydrogenations. *Science* 2012; **335**: 1209–12.
6. Sun S, Zhang G and Gauquelin N *et al.* Single-atom catalysis using Pt/graphene achieved through atomic layer deposition. *Sci Rep* 2013; **3**: 1775.
7. Taylor HS. A theory of the catalytic surface. *Proc R Soc London Ser A* 1925; **108**: 105–11.
8. Wang Y, Wang X and Antonietti M. Polymeric graphitic carbon nitride as a heterogeneous organocatalyst: from photochemistry to multipurpose catalysis to sustainable chemistry. *Angew Chem Int Ed* 2012; **51**: 68–89.
9. Thomas A, Fischer A and Goettmann F *et al.* Graphitic carbon nitride materials: variation of structure and morphology and their use as metal-free catalysts. *J Mater Chem* 2008; **18**: 4893–908.
10. Liu AY and Cohen ML. Prediction of new low compressibility solids. *Science* 1989; **245**: 841–2.
11. Molina B and Sansores LE. Electronic structure of six phases of C_3N_4: a theoretical approach. *Mod Phys Lett B* 1999; **13**: 193–201.

12. Lin Z and Wang X. Nanostructure engineering and doping of conjugated carbon nitride semiconductors for hydrogen photosynthesis. *Angew Chem Int Ed* 2013; **52**: 1735–8.
13. Wang X, Chen X and Thomas A *et al.* Metal-containing carbon nitride compounds: a new functional organic–metal hybrid material. *Adv Mater* 2009; **21**: 1609–12.
14. Chen X, Zhang J and Fu X *et al.* Fe-g-C_3N_4-catalyzed oxidation of benzene to phenol using hydrogen peroxide and visible light. *J Am Chem Soc* 2009; **131**: 11658–9.
15. Kroke E, Schwarz M and Horath-Bordon E *et al.* Tri-s-triazine derivatives. Part I. From trichloro-tri-s-triazine to graphitic C_3N_4 structures. *New J Chem* 2002; **26**: 508–12.
16. Liu J, Wang H and Antonietti M. Graphitic carbon nitride 'reloaded': emerging applications beyond (photo)catalysis. *Chem Soc Rev* 2016; **45**: 2308–26.
17. Chen ZP, Antonietti M and Dontsova D. Enhancement of the photocatalytic activity of carbon nitrides by complex templating. *Chem Eur J* 2015; **21**: 10805–11.
18. Fina F, Callear SK and Carins GM *et al.* Structural investigation of graphitic carbon nitride via XRD and neutron diffraction. *Chem Mater* 2015; **27**: 2612–8.
19. Wang X, Maeda K and Thomas A *et al.* A metal-free polymeric photocatalyst for hydrogen production from water under visible light. *Nat Mater* 2009; **8**: 76–80.
20. Sattler A, Pagano S and Zeuner M *et al.* Melamine-melem adduct phases: investigating the thermal condensation of melamine. *Chem Eur J* 2009; **15**: 13161–70.
21. Kessler FK, Zheng Y and Schwarz D *et al.* Functional carbon nitride materials-design strategies for electrochemical devices. *Nat Rev Mater* 2017; **2**: 17030.
22. Doblinger M, Lotsch BV and Wack J *et al.* Structure elucidation of polyheptazine imide by electron diffraction-a templated 2D carbon nitride network. *Chem Commun* 2009; 1541–3.
23. Wirnhier E, Döblinger M and Gunzelmann D *et al.* Poly(triazine imide) with intercalation of lithium and chloride ions $[(C_3N_3)_2(NH_xLi_{1-x})_3 \bullet LiCl]$: a crystalline 2d carbon nitride network. *Chem Eur J* 2011; **17**: 3213–21.
24. Bojdys MJ, Müller J-O and Antonietti M *et al.* Ionothermal synthesis of crystalline, condensed, graphitic carbon nitride. *Chem Eur J* 2008; **14**: 8177–82.
25. Dontsova D, Pronkin S and Wehle M *et al.* Triazoles: a new class of precursors for the synthesis of negatively charged carbon nitride derivatives. *Chem Mater* 2015; **27**: 5170–9.
26. Savateev A, Dontsova D and Kurpil B *et al.* Highly crystalline poly(heptazine imides) by mechanochemical synthesis for photooxidation of various organic substrates using an intriguing electron acceptor-elemental sulfur. *J Catal* 2017; **350**: 203–11.
27. Liang Q, Huang Z-H and Kang F *et al.* Facile synthesis of crystalline polymeric carbon nitrides with an enhanced photocatalytic performance under visible light. *ChemCatChem* 2015; **7**: 2897–902.
28. Chen Z, Savateev A and Pronkin S *et al.* 'The easier the better' preparation of efficient photocatalysts-metastable poly(heptazine imide) salts. *Adv Mater* 2017; **29**: 1700555.
29. Vilé G, Albani D and Nachtegaal M *et al.* A stable single-site palladium catalyst for hydrogenations. *Angew Chem Int Ed* 2015; **54**: 11265–9.
30. Chen Z, Pronkin S and Fellinger T-P *et al.* Merging single-atom-dispersed silver and carbon nitride to a joint electronic system via copolymerization with silver tricyanomethanide. *ACS Nano* 2016; **10**: 3166–75.
31. Li X, Bi W and Zhang L *et al.* Single-atom Pt as co-catalyst for enhanced photocatalytic H_2 evolution. *Adv Mater* 2016; **28**: 2427–31.
32. Huang X, Xia Y and Cao Y *et al.* Enhancing both selectivity and coking-resistance of a single-atom Pd_1/C_3N_4 catalyst for acetylene hydrogenation. *Nano Res* 2017; **10**: 1302–12.
33. Chen Z, Mitchell S and Vorobyeva E *et al.* Stabilization of single metal atoms on graphitic carbon nitride. *Adv Funct Mater* 2017; **27**: 1605785.
34. Liu W, Cao L and Cheng W *et al.* Single-site active cobalt-based photocatalyst with a long carrier lifetime for spontaneous overall water splitting. *Angew Chem Int Ed* 2017; **56**: 9312–7.
35. Vorobyeva E, Chen Z and Mitchell S *et al.* Tailoring the framework composition of carbon nitride to improve the catalytic efficiency of the stabilised palladium atoms. *J Mater Chem A* 2017; **5**: 16393–403.
36. Zheng Y, Jiao Y and Zhu Y *et al.* Molecule-level g-C_3N_4 coordinated transition metals as a new class of electrocatalysts for oxygen electrode reactions. *J Am Chem Soc* 2017; **139**: 3336–9.
37. Lau VW-h, Mesch MB and Duppel V *et al.* Low-molecular-weight carbon nitrides for solar hydrogen evolution. *J Am Chem Soc* 2015; **137**: 1064–72.
38. Lotsch BV, Döblinger M and Sehnert J *et al.* Unmasking melon by a complementary approach employing electron diffraction, solid-state NMR spectroscopy, and theoretical calculations-structural characterization of a carbon nitride polymer. *Chem Eur J* 2007; **13**: 4969–80.
39. Zimmerman JL, Williams R and Khabashesku VN *et al.* Synthesis of spherical carbon nitride nanostructures. *Nano Lett* 2001; **1**: 731–4.
40. Komatsu T. Attempted chemical synthesis of graphite-like carbon nitride. *J Mater Chem* 2001; **11**: 799–801.
41. Chong SY, Jones JTA and Khimyak YZ *et al.* Tuning of gallery heights in a crystalline 2D carbon nitride network. *J Mater Chem A* 2013; **1**: 1102–7.
42. Yan H, Cheng H and Yi H *et al.* Single-atom Pd_1/graphene catalyst achieved by atomic layer deposition: remarkable performance in selective hydrogenation of 1,3-butadiene. *J Am Chem Soc* 2015; **137**: 10484–7.
43. Jun Y-S, Lee EZ and Wang X *et al.* From melamine-cyanuric acid supramolecular aggregates to carbon nitride hollow spheres. *Adv Funct Mater* 2013; **23**: 3661–7.
44. Vernuccio S, von Rohr PR and Medlock J. General kinetic modeling of the selective hydrogenation of 2-methyl-3-butyn-2-ol over a commercial palladium-based catalyst. *Ind Eng Chem Res* 2015; **54**: 11543–51.
45. Kresse G and Furthmüller J. Efficient iterative schemes for ab initio total-energy calculations using a plane-wave basis set. *Phys Rev B* 1996; **54**: 11169–86.
46. Perdew JP, Chevary JA and Vosko SH *et al.* Atoms, molecules, solids, and surfaces: applications of the generalized gradient approximation for exchange and correlation. *Phys Rev B* 1992; **46**: 6671–87.
47. Grimme S, Antony J and Ehrlich S *et al.* A consistent and accurate ab initio parametrization of density functional dispersion correction (DFT-D) for the 94 elements H-Pu. *J Chem Phys* 2010; **132**: 154104.
48. Kresse G and Joubert D. From ultrasoft pseudopotentials to the projector augmented-wave method. *Phys Rev B* 1999; **59**: 1758–75.
49. Heyd J, Scuseria GE and Ernzerhof M. Hybrid functionals based on a screened coulomb potential. *J Chem Phys* 2003; **118**: 8207–15.
50. Álvarez-Moreno M, de Graaf C and López N *et al.* Managing the computational chemistry big data problem: the ioChem-BD platform. *J Chem Inf Model* 2015; **55**: 95–103.